

# Moiré-regulated composition evolution kinetics of bicomponent nanoclusters

Mikhail Khenner<sup>a1,2</sup>

<sup>1</sup>*Department of Mathematics, Western Kentucky University, Bowling Green, KY 42101, USA*

<sup>2</sup>*Applied Physics Institute, Western Kentucky University, Bowling Green, KY 42101, USA*

(Dated: October 25, 2024)

A simple model and computation of Moiré-regulated composition evolution kinetics of bicomponent nanoclusters is presented. Assuming continuous adsorbate coverage on top of 2D bilayer and Moiré potential-driven nanocluster formation at fcc sites of Moiré landscape, these sites experience the influx of one component of a bicomponent adsorbate and the outflux of another component. Kinetics of this process is characterized for several combinations of adsorption potentials and their relative strengths.

*Keywords:* Bimetallic nanoclusters and nanoparticles; Moiré-regulated self-assembly; Directed self-assembly.

## I. INTRODUCTION

Bilayers of 2D materials, such as twisted bilayer graphene, or a single-layer 2D material (e.g., graphene) deposited onto a high-symmetry surface of a noble metal, feature a biperiodic structure of hills and valleys known as Moiré superlattice. This structure gives rise to spatially selective adsorption of atoms or molecules and it also presents a complex landscape for surface diffusion. Therefore, Moiré-regulated self-assembly has been widely used to create ordered 2D arrays of a single-metallic nanoclusters and nanoparticles [1]-[12]. Less known is that bimetallic nanoclusters and nanoparticles also can be fabricated using this technique [13]-[15]. These authors prepared the substrate size (up to 1 cm<sup>2</sup>) regular arrays of PdAu alloy nanoclusters on nanostructured ultrathin alumina films [13], PtRu alloy nanoclusters on graphene/Ru(0001) [14], and PdPt alloy nanoclusters on graphene/Rh(111) [15]. They demonstrated an independent control of the nanocluster size and its chemical composition by controlling the total amounts and the ratio of deposited metals. Also they demonstrated the narrow size distribution of the nanoclusters. The latter has been shown due to the regular distribution of the nucleation centers, which results in the uniform cluster growth rate. Notably, the metals may be deposited sequentially [13, 14] or simultaneously [15]. These studies pave the way to the studies of the reactivity of bimetallic clusters as a function of the composition at a given size, which is important for catalysis. Regular bimetallic nanocluster arrays serve as high-quality model nanocatalysts, allowing to study electrocatalytic oxidation reactions, sintering, poisoning, or to stabilize species like aldehydes. Notably, two fundamental electrocatalytic reactions in polymer electrolyte membrane fuel cells are the oxidation of CO [15] or methanol.

In this short communication we build upon our model of nanocluster self-assembly on graphene Moiré [16] and our modeling of composition patterning in bimetallic surface alloys [17]-[19], to compute Moiré-regulated composition evolution kinetics of bicomponent nanoclusters. We deliberately keep the modeling generic, i.e. we do not assume a concrete bilayer substrate and a pair of metals that form a bimetallic nanocluster array. For proof of concept, we construct a primitive Moiré potential via the rotation (twist) of a top unstrained honeycomb lattice with respect to the identical unstrained bottom lattice. Next, we formulate evolution equation for the space and time-dependent composition of a bicomponent adsorbate that is driven by Moiré potential and, starting from a spatially uniform composition, quantify evolution kinetics of nanocluster composition.

## II. THE MODEL

### A. Moiré potential

Dimensionless Moiré potential is given by [16, 20, 21]:

$$\epsilon_m(x, y) = \frac{1}{3} \sqrt{3 + 2 [\cos \mathbf{x} \cdot \mathbf{c}_1 + \cos \mathbf{x} \cdot \mathbf{c}_2 + \cos \mathbf{x} \cdot (\mathbf{c}_1 - \mathbf{c}_2)]}, \quad (1)$$

$$\mathbf{c}_1 = M^{-1} \left( 1/2, \sqrt{3}/2 \right)^T, \quad \mathbf{c}_2 = M^{-1} \left( -1/2, \sqrt{3}/2 \right)^T, \quad \mathbf{x} = \left( -\frac{4\pi}{3}x, \frac{4\pi}{3}y \right). \quad (2)$$

---

<sup>a</sup> Corresponding author. E-mail: mikhail.khenner@wku.edu.

Here the (antisymmetric) scale matrix  $M$  for unstrained 2D bilayer is:

$$M = \begin{pmatrix} 0 & \frac{1}{\theta} \\ -\frac{1}{\theta} & 0 \end{pmatrix}, \quad (3)$$

where  $\theta$  is the twist angle of a (honeycomb) top atomic lattice with respect to a (honeycomb) bottom atomic lattice in a bilayer. The lattices are assumed identical, i.e. they represent the same 2D material. The effect of the rotation is the magnification of the bottom lattice and the emergence of a large-scale Moiré structure with a potential (1). Fig. 1(b) shows Moiré potential that results from  $8^\circ$  counter-clockwise rotation. The plotting window corresponds to the actual biperiodic domain used to compute Moiré-regulated composition evolution kinetics of a bicomponent adsorbate. Note that the computational domain contains five complete Moiré cells. The unit of length in Fig. 1 is equal to graphene lattice spacing  $a_g$ . Also we chose to have the minima of Moiré potential at fcc sites of Moiré lattice, and correspondingly, the maxima are at top sites, as this is the most common situation across bilayer substrates in experiment [1]-[12]. This choice implies nanocluster formation at fcc sites; the modeling aims to compute evolution kinetics of nanocluster composition at these sites.

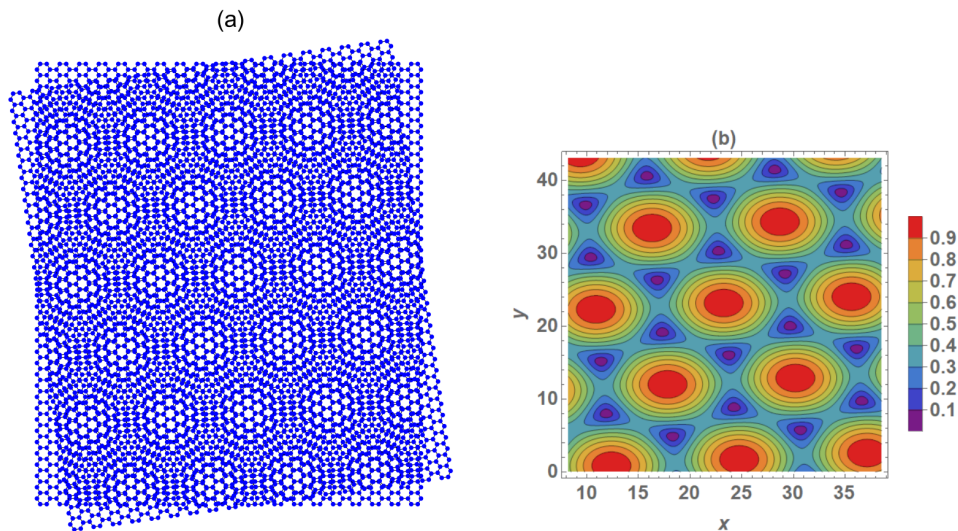


FIG. 1. (a) Moiré formed by two identical hexagonal lattices rotated by  $8^\circ$ . (b) Corresponding Moiré potential  $\epsilon_m(x, y)$ . Red regions are top sites, blue regions are fcc sites.

Adsorption potentials  $\epsilon_a^{(I)}(x, y)$  and  $\epsilon_a^{(II)}(x, y)$  of two atomic species at the top layer of a bilayer substrate are given by the expressions similar to Eq. (2):

$$\epsilon_a^{(I)}(x, y) = \frac{1}{3} \sqrt{3 + 2 [\cos \mathbf{x} \cdot \mathbf{c}_1 + \cos \mathbf{x} \cdot \mathbf{c}_2 + \cos \mathbf{x} \cdot (\mathbf{c}_1 - \mathbf{c}_2)]}, \quad (4)$$

$$\mathbf{c}_1 = \left(1/2, \sqrt{3}/2\right)^T, \quad \mathbf{c}_2 = \left(-1/2, \sqrt{3}/2\right)^T, \quad \mathbf{x} = \left(-\frac{4\pi}{3}x, \frac{4\pi}{3}y\right), \quad (5)$$

$$\epsilon_a^{(II)}(x, y) = 1 - \epsilon_a^{(I)}(x, y). \quad (6)$$

Notice that the scale matrix  $M$  is absent from the vectors  $\mathbf{c}_1$  and  $\mathbf{c}_2$ , since adsorption takes place on the top 2D layer of a bilayer substrate, whereby small atomic cells determine the adsorption sites. (Equivalently,  $M = I$ , where  $I$  is  $2 \times 2$  identity matrix.) Figures 2(a,b) show these adsorption potentials in a correspondingly smaller biperiodic plotting window. The first atomic species (either A or B) preferentially adsorbs at fcc sites on the top 2D layer of a bilayer substrate, whereas the second atomic species preferentially adsorbs at top sites. For comparison of vastly different scales of Moiré and the adsorption potentials, Fig. 2(c) shows the 0.1 level set plot of  $\epsilon_a^{(I)}(x, y)$  overlaid onto Moiré potential  $\epsilon_m(x, y)$  in the computational window. The 0.1 level set contains the minima of  $\epsilon_a^{(I)}(x, y)$ , i.e. it shows the locations of fcc adsorption sites on the top 2D layer of a bilayer substrate.

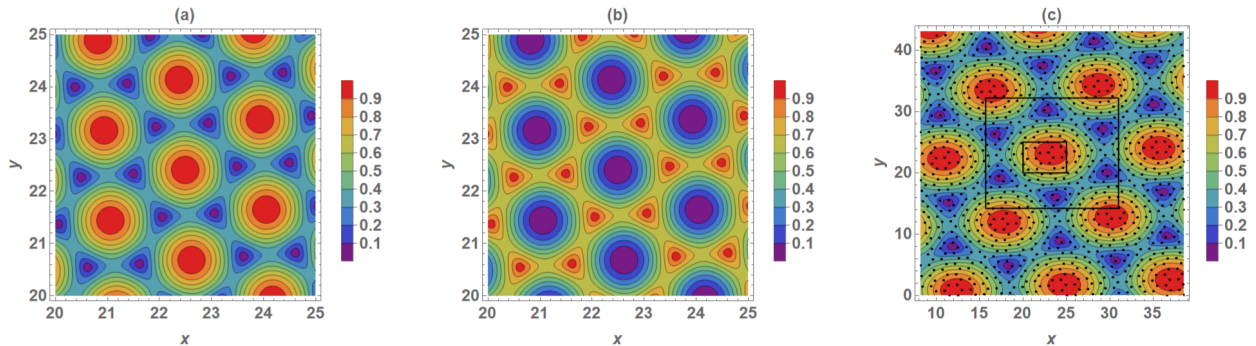


FIG. 2. Adsorption potentials (a)  $\epsilon_a^{(I)}(x, y)$  and (b)  $\epsilon_a^{(II)}(x, y)$ . (c) shows the 0.1 level set plot of  $\epsilon_a^{(I)}(x, y)$  (the tiny black ovals resembling points) overlaid onto Moiré potential  $\epsilon_m(x, y)$ . Smaller frame corresponds to the plotting window of the panels (a) and (b). Larger frame marks a single Moiré cell.

## B. Evolution equation for Moiré-regulated composition of bicomponent nanoclusters

In this section we formulate equation that models composition evolution kinetics of a bicomponent adsorbate (a binary mixture) on a Moiré formed by two mutually rotated 2D honeycomb atomic lattices. A Moiré of unstrained twisted bilayer graphene is used as example.

Let  $\nu_A$  and  $\nu_B$  be the surface densities, or the surface concentrations (compositions) of A and B adsorbate components (shortened to A and B adsorbates in the rest of the paper) immediately after deposition on the top of 2D bilayer. Let also  $X_A(x, y, t)$  and  $X_B(x, y, t)$  be the local time-dependent surface concentrations in the course of nanocluster directed self-assembly. Define the dimensionless local time-dependent concentrations as  $C_A(x, y, t) = X_A/\nu_A$  and  $C_B(x, y, t) = X_B/\nu_B$ . Mass conservation requires  $C_A(x, y, t) + C_B(x, y, t) = 1$ , and without significant loss of generality we assume  $\nu_A = \nu_B = \nu$  to reduce the number of dimensionless parameters. We choose  $a_g$  and  $a_g^2 kT\nu/D_B\gamma_B$  for the length and time scales, respectively. Here  $a_g$  is graphene lattice spacing,  $kT$  is Boltzmann's factor, and  $D_B$ ,  $\gamma_B$  are the surface diffusivity and the surface energy of B adsorbate.

According to classical irreversible thermodynamics the dimensionless evolution equation for the concentration of B adsorbate reads:

$$\frac{\partial C_B}{\partial t} = \nabla \cdot (L_{AB} \nabla \mu_A + L_{BB} \nabla \mu_B), \quad (7)$$

where  $L_{AB}$ ,  $L_{BB}$  are the kinetic transport coefficients and  $\mu_A$  and  $\mu_B$  the chemical potentials. The latter are given by [22, 23]:

$$\mu_A = -C_B \frac{\partial \gamma}{\partial C_B} + \xi_A \nabla^2 C_B + \Omega \epsilon_m(x, y), \quad (8)$$

$$\mu_B = (1 - C_B) \frac{\partial \gamma}{\partial C_B} - \xi_B \nabla^2 C_B + \Omega \epsilon_m(x, y), \quad (9)$$

where

$$\gamma = G(1 - C_B) + C_B + N[(1 - C_B) \ln(1 - C_B) + C_B \ln C_B + HC_B(1 - C_B)] \quad (10)$$

is the free energy [23–26]. In Eqs. (8), (9)  $\Omega$  is the strength of Moiré potential. In Eq. (10) the first two terms constitute the weighted surface energy of a bicomponent monolayer [26]. Also, the first two terms in the bracket are the entropic contributions, and the last term in the bracket is the enthalpic contribution [27]. Together, the three terms in the bracket are the regular solution model. All physical and dimensionless parameters are shown in Table I.

The kinetic transport coefficients are [16, 18, 23]:

$$L_{AB} = D e^{F_A \alpha(x, y)} C_B (1 - C_B), \quad L_{BB} = e^{F_B \beta(x, y)} C_B^2, \quad (11)$$

where  $\alpha(x, y)$ ,  $\beta(x, y)$  are the placeholders for the adsorption potentials [28]. Thus  $\alpha(x, y)$  or  $\beta(x, y)$  can be assigned either  $\epsilon_a^{(I)}(x, y)$  or  $\epsilon_a^{(II)}(x, y)$ . Notice that the potentials  $\epsilon_m(x, y)$ ,  $\epsilon_a^{(I)}(x, y)$ , and  $\epsilon_a^{(II)}(x, y)$  have the same dimensionless depth one (see Fig. 2); the strengths of the potentials are set by the parameters  $\Omega$ ,  $F_A$ , and  $F_B$ .  $F_A$  and  $F_B$  are the

inverses of the adsorbate-substrate binding energies.  $De^{F_A\alpha(x,y)}$  and  $e^{F_B\beta(x,y)}$  are the diffusional mobilities of two atom species which comprise a bicomponent adsorbate.

Eq. (7) is of an extended forced Cahn-Hilliard (CH) type. A typical value of the enthalpy  $H$  (see Table I) precludes a thermodynamically driven phase separation (a spinodal instability) of a binary mixture. Thus changes in the composition of bicomponent nanoclusters are expected to be caused by forced phase separation that is driven by Moiré potential. Cahn-Hilliard gradient energy terms  $\xi_A \nabla^2 C_B$  and  $-\xi_B \nabla^2 C_B$  in the chemical potentials (8) and (9) account for adsorbate-adsorbate interactions [16].

Physical parameter and typical value	Dimensionless parameter and value
Graphene lattice spacing, $a_g = 2.46 \times 10^{-8}$ cm	
Lattice spacing of A adsorbate, $a_A = 3.92 \times 10^{-8}$ cm	
Lattice spacing of B adsorbate, $a_B = 2.7 \times 10^{-8}$ cm	
Temperature, $T = 20^\circ$	
Surface energy of A adsorbate, $\gamma_A = 2.3 \times 10^3$ erg/cm <sup>2</sup> [29]	
Surface energy of B adsorbate, $\gamma_B = 1.17 \times 10^3$ erg/cm <sup>2</sup> [29]	Ratio of surface energies, $G = \gamma_A/\gamma_B = 1.96$
Surface density of either A or B adsorbate, $\nu = a_g^{-2} = 1.65 \times 10^{15}$ cm <sup>-2</sup>	Entropy, $N = kT\nu/\gamma_B = 0.022$
Strength of Moiré potential, $\delta = 1.2 \times 10^{-11}$ erg	Strength of Moiré potential, $\Omega = \delta\nu/\gamma_B = 6.52$
CH gradient energy coefficient, $\kappa = 1.2 \times 10^{-5}$ erg/cm [30]	CH gradient energy parameter, $\xi_A = \kappa a_A/a_g^2 \gamma_B = 0.66$
	CH gradient energy parameter, $\xi_B = \kappa a_B/a_g^2 \gamma_B = 0.46$
Enthalpy of a binary mixture, $\eta = 0.01\gamma_B = 11.7$ erg/cm <sup>2</sup>	Enthalpy, $H = \eta/kT\nu = 0.45$
	Ratio of surface diffusivities, $D = D_A/D_B$ (varies)

TABLE I. Physical and dimensionless parameters.  $a_A$  and  $a_B$  correspond to Pt and Ru, respectively.  $D_A$ ,  $D_B$ , and the strengths of the adsorption potentials are not shown in the physical parameter column, since only the ratio  $D = D_A/D_B$  and the dimensionless strengths  $F_A$  and  $F_B$  of the adsorption potentials are required.

### C. Results

Eq. (7) is computed using a Method of Lines framework. Spatial discretization on a fine 256x256 grid is via the fourth-order finite differences, the time integration is done by the implicit midpoint method. The logarithmic terms in the free energy are handled by the technique described in Ref. [19]. The initial condition is  $C_B(x, y) = 0.1$  at  $t = 0$ , i.e. a binary mixture has 10% of B atoms spread uniformly over Moiré landscape shown in Fig. 1.

We select six cases 1(a)-3(b) as follows:

1.  $F_A = 0$ ,  $F_B = 1.5$

(a)  $\beta(x, y) = \epsilon_a^{(I)}(x, y)$

(b)  $\beta(x, y) = \epsilon_a^{(II)}(x, y)$

2.  $F_A = 1.5$ ,  $F_B = 0$

(a)  $\alpha(x, y) = \epsilon_a^{(I)}(x, y)$

(b)  $\alpha(x, y) = \epsilon_a^{(II)}(x, y)$

3.  $F_A = F_B = 1.5$

(a)  $\alpha(x, y) = \epsilon_a^{(I)}(x, y)$ ,  $\beta(x, y) = \epsilon_a^{(II)}(x, y)$

(b)  $\alpha(x, y) = \epsilon_a^{(II)}(x, y)$ ,  $\beta(x, y) = \epsilon_a^{(I)}(x, y)$

For each case we also vary the ratio of the surface diffusivities,  $D$ . Note that the cases 1(a,b) correspond to A atom having equal probability to adsorb at fcc or top site on the top layer of a bilayer substrate, whereas the cases 2(a,b) correspond to B atom having equal probability to adsorb at fcc or top site. Value 1.5 for  $F_A$  and  $F_B$  is chosen because at larger  $F_A$  or  $F_B$  the excessive numerical stiffness makes the computation of Eq. (7) prohibitively slow.

As the example, for cases 1(a), 2(a), and 3(a) Fig. 3 shows the distribution of the concentration of B adsorbate in the central Moiré cell shortly after Moiré-regulated self-assembly has begun. Significant differences can be observed only due to differences in the mobilities of the adsorbate components that are caused by the choices of the adsorption potentials. Note that the maximum and minimum values of  $C_B$  also differ. Under the action of Moiré potential B adsorbate is driven out of the top site, i.e. out of the center of the Moiré cell and it starts to accumulate at fcc sites. With time, its concentration at fcc sites steadily increases, while the concentration at the top site steadily decreases. Correspondingly, the concentration of A adsorbate increases at the top site and decreases at fcc sites. Moiré-regulated self-assembly would terminate when B adsorbate depletes entirely at the top site ( $C_B = 0, C_A = 1$ ) and correspondingly at fcc sites  $C_B = 1, C_A = 0$ .

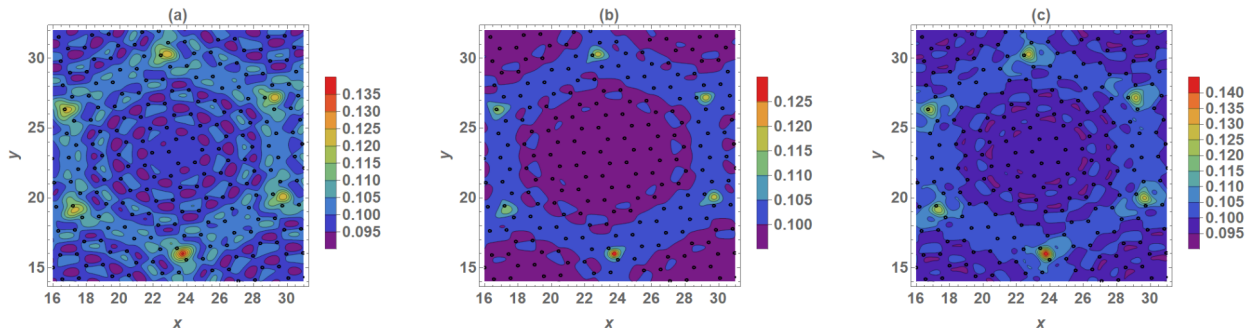


FIG. 3.  $C_B(x, y)$  at  $t = 0.02$  in the Moiré cell framed in Fig. 2(c).  $D = 1$ . (a) Case 1(a), (b) Case 2(a), (c) Case 3(a). The tiny black ovals show the 0.1 level set of  $\epsilon_a^{(I)}(x, y)$ .

$C_B$  increases at nearly the same rate at all fcc sites in the computational domain (Fig. 1). In Fig. 4 the typical spatial profile of  $C_B$  over an fcc site is shown at three time instances. The profile broadens with time, whilst the maximum of  $C_B$ , attained at the site center, increases with time.

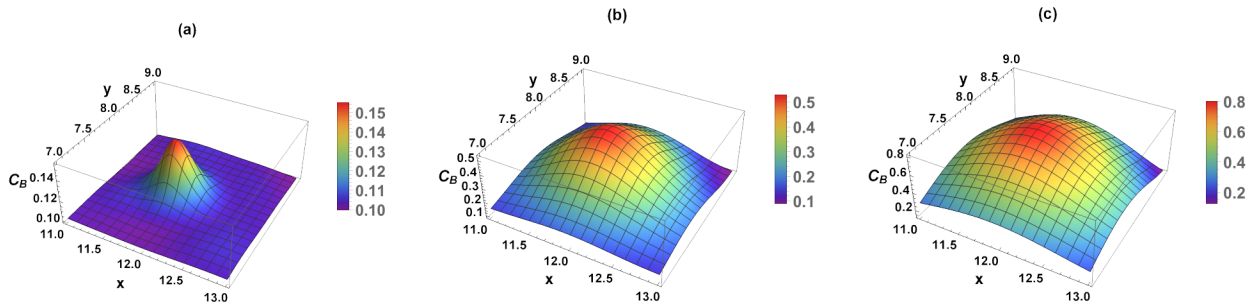


FIG. 4.  $C_B(x, y)$  across an fcc site for Case 2(a). (a)  $t = 0.02$ , (b)  $t = 0.5$ , (c)  $t = 1$ .

To characterize the kinetics of nanocluster composition evolution, we choose one of fcc sites and in Fig. 5 plot  $C_B$  value at the site center as function of time. We observe that cases 3(b) and 1(b) provide the most efficient nanocluster enrichment by B component, with a weak dependence on  $D$  (see the green and purple curves in Figures 5(b), (d), (e)). For these cases  $F_B = 1.5$  and therefore the mobility of B adsorbate is large. Cases 2(a), 2(b) provide the least efficient nanocluster enrichment by B component, with stronger dependence on  $D$  (see Figures 5(a)-(d)). For these cases  $F_B = 0$  and therefore transport of B adsorbate is slow. As  $D$  decreases, also the mobility of A adsorbate decreases. This leads to weaker outflow of A component from nanoclusters, and therefore nanocluster enrichment by B component slows down (compare the brown curves in Figures 5(a),(c) and the red curves in Figures 5(b),(d)).

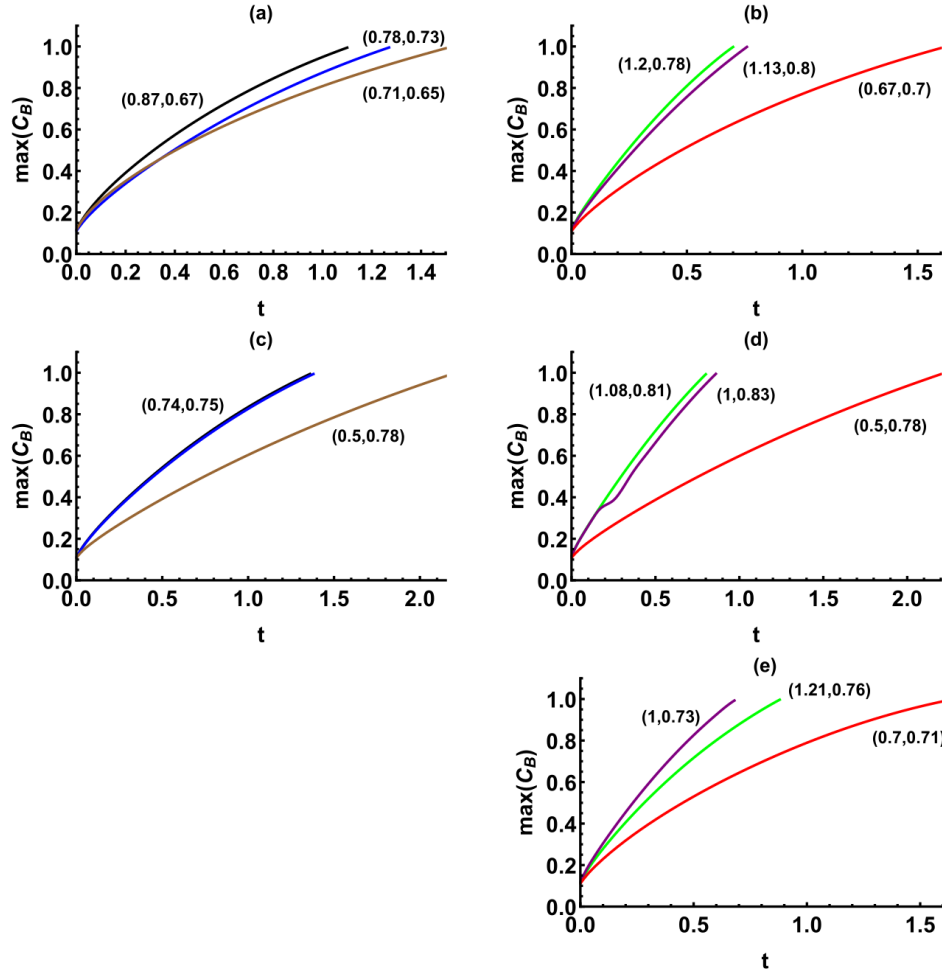


FIG. 5. Maximum of  $C_B(x, y)$  at an fcc site vs. time. (a) Case 3(a) (black curve), Case 1(a) (blue curve), Case 2(a) (brown curve) at  $D = 1$ ; (b) Case 3(b) (green curve), Case 1(b) (purple curve), Case 2(b) (red curve) at  $D = 1$ ; (c) Case 3(a) (black curve), Case 1(a) (blue curve), Case 2(a) (brown curve) at  $D = 0.1$ ; (d) Case 3(b) (green curve), Case 1(b) (purple curve), Case 2(b) (red curve) at  $D = 0.1$ ; (e) Case 3(b) at  $D = 1.75$  (green curve), Case 1(b) at  $D = 2.5$  (purple curve), Case 2(b) at  $D = 1.1$  (red curve). All curves are the fits to data of the form  $\max(C_B) = 0.1 + rt^z$ ; the pair  $(r, z)$  is marked next to each curve.

### III. CONCLUSIONS

This paper presents a generic kinetic model for a continuous bicomponent adsorbate that is driven by Moiré potential. Moiré-regulated surface diffusion results in nanoclusters whose composition strongly depends on time and on the details and strength of the adsorption potentials of two atom species at the top layer of a 2D bilayer substrate. Typically, if the adsorbate-substrate binding energy of one adsorbate component is weak, then the corresponding diffusional mobility is strong, and a nanocluster becomes enriched by that component. Kinetics of such enrichment follows a power law in time, with the exponent in the range 0.7-0.83.

### DECLARATIONS

**Ethical Approval**  
Not applicable.

**Funding**

No funding was received for this research.

- 
- [1] A.T. N'Diaye, S. Bleikamp, P.J. Feibelman, and T. Michely, “Two-Dimensional Ir Cluster Lattice on a Graphene Moiré on Ir(111)”, *Phys. Rev. Lett.* **97**, 215501 (2006).
- [2] A.T. N'Diaye, T. Gerber, C. Busse, J. Myslivecek, J. Coraux, and T. Michely, “A versatile fabrication method for cluster superlattices”, *New. J. Phys.* **11**, 103045 (2009).
- [3] M.D. Jimenez-Sanchez, C. Romero-Muniz, P. Pou, R. Perez, and J.M. Gomez-Rodriguez, “Graphene on Rh(111): A template for growing ordered arrays of metal nanoparticles with different periodicities”, *Carbon* **173**, 1073e1081 (2021).
- [4] X. Liu, Y. Han, J.W. Evans, A.K. Engstfeld, R.J. Behm, M.C. Tringides, M. Hupalo, H.-Q. Lin, L. Huang, K.-M. Ho, D. Appy, P.A. Thiel, and C.-Z. Wang, “Growth morphology and properties of metals on graphene”, *Prog. Surf. Sci.* **90**, 397 (2015).
- [5] A.K. Engstfeld, H.E. Hoster, R.J. Behm, L.D. Roelofs, X. Liu, C.-Z. Wang, Y. Han, and J.W. Evans, “Directed assembly of Ru nanoclusters on Ru(0001)-supported graphene: STM studies and atomistic modeling”, *Phys. Rev. B* **86**, 085442 (2012).
- [6] Y. Pan, M. Gao, L. Huang, F. Liu, and H.-J. Gao, “Directed self-assembly of monodispersed platinum nanoclusters on graphene Moiré template”, *Appl. Phys. Lett.* **95**, 093106 (2009).
- [7] M. Sicot, S. Bouvron, O. Zander, U. Rudiger, Vu.S. Dedkov, and M. Fonin, “Nucleation and growth of nickel nanoclusters on graphene Moiré on Rh(111)”, *Appl. Phys. Lett.* **96**, 093115 (2010).
- [8] Z. Zhou, F. Gao, and D.W. Goodman, “Deposition of metal clusters on single-layer graphene/Ru(0001): Factors that govern cluster growth”, *Surf. Sci.* **604**, L31 (2010).
- [9] K. Donner and P. Jakob, “Structural properties and site specific interactions of Pt with the graphene/Ru(0001) moiré overlayer”, *J. Chem. Phys.* **131**, 164701 (2009).
- [10] L. W. Liu, W. D. Xiao, K. Yang, L. Z. Zhang, Y. H. Jiang, X. M. Fei, S. X. Du, and H.-J. Gao, “Growth and Structural Properties of Pb Islands on Epitaxial Graphene on Ru(0001)”, *J. Phys. Chem.* **117**, 22652 (2013).
- [11] L. Semidey-Flecha, D. Teng, B.F. Habenicht, D.S. Sholl, and Y. Xu, “Adsorption and diffusion of the Rh and Au adatom on graphene moiré/Ru(0001)”, *J. Chem. Phys.* **138**, 184710 (2013).
- [12] M. Petrovic, P. Lazic, S. Runte, T. Michely, C. Busse, and M. Kralj, “Moiré-regulated self-assembly of cesium adatoms on epitaxial graphene”, *Phys. Rev. B* **96**, 085428 (2017).
- [13] M. Marsault, G.H.A. Worz, G. Sitja, C. Barth, and C. R. Henry, “Preparation of regular arrays of bimetallic clusters with independent control of size and chemical composition”, *Faraday Discussions* **138**, 407 (2008).
- [14] A.K. Engstfeld, S. Beckord, C.D. Lorenz, and R.J. Behm, “Growth of PtRu Clusters on Ru(0001)-Supported Monolayer Graphene Films”, *Chem. Phys. Chem.* **13**, 3313 (2012).
- [15] F. Dull, U. Bauer, F. Spath, P. Bachmann, J. Steinhauer, H.-P. Steinruck, and C. Papp, “Bimetallic Pd–Pt alloy nanocluster arrays on graphene/Rh(111): formation, stability, and dynamics”, *Phys. Chem. Chem. Phys.*, **20**, 21294 (2018).
- [16] M. Khenner and L. Hebenstiel, “A mesoscopic model of nanoclusters self-assembly on a graphene Moiré”, *J. Appl. Phys.* **130**, 124301 (2021).
- [17] M. Khenner, “Electromigration-guided composition patterns in thin alloy films: a computational study”, *Surf. Sci.* **698**, 121611 (2020).
- [18] M. Khenner, “Directed long-range transport of a nearly pure component atom clusters by the electromigration of a bimetallic surface alloy”, *Phys. Rev. Materials* **5**, 024001 (2021).
- [19] M. Khenner, “Vacancy-mediated suppression of phase separation in a model two-dimensional surface alloy by the difference of the atomic jump rates”, *Surf. Sci.* **722**, 122100 (2022).
- [20] D.A. Cosma, J.R. Wallbank, V. Cheianov, and V.I. Fal’ko, “Moiré pattern as a magnifying glass for strain and dislocations in van der Waals heterostructures”, *Faraday Discussions* **173**, 137 (2014).
- [21] J.F. Wallbank, M. Mucha-Kruczynski, X. Chen, and V.I. Fal’ko, “Moiré superlattice effects in graphene/boronitride van der Waals heterostructures”, *Annalen der Physik* **527**, 359-376 (2015).
- [22] Q. Zhang, P.W. Voorhees, and S.H. Davis, “Mechanisms of surface alloy segregation on faceted core-shell nanowire growth”, *J. Mech. Phys. Solids* **100**, 21-44 (2017).
- [23] R. Raghavan, P. Wu, and K. Ankit, “Phase-field modeling of nanostructural evolution in physical vapor deposited phase-separating ternary alloy films”, *Modelling Simul. Mater. Sci. Eng.* **30**, 084004 (2022).
- [24] Z. Suo and W. Lu, “Forces that Drive Nanoscale Self-Assembly on Solid Surfaces”, *J. Nanoparticle Res.*, **2**, 333 (2000).
- [25] W. Lu and D. Kim, “Engineering nanophase self-assembly with elastic field”, *Acta Mater.* **53**, 3689 (2005).
- [26] A.V. Ruban, H.L. Skriver, and J.K. Norskov, “Local equilibrium properties of metallic surface alloys”, in: *The Chemical Physics of Solid Surfaces*, Ed.: D.P. Woodruff, vol. 10, Elsevier (2002).
- [27] A. De Virgiliis and K. Binder, “Interplay of order-disorder phenomena and diffusion in rigid bimetallic alloys in the presence of vacancies: Monte Carlo simulations”, *Phys. Rev. B* **73**, 134205 (2006).
- [28] D.G. Vlachos and M.K. Katsoulakis, “Derivation and validation of mesoscopic theories for diffusion of interacting molecules”, *Phys. Rev. Lett.* **85**, 3898 (2000).
- [29] L. Vitos, A.V. Ruban, H.L. Skriver, and J. Kolla, “The surface energy of metals”, *Surf. Sci.* **411**, 186-202 (1998).
- [30] J.J. Hoyt, “Molecular dynamics study of equilibrium concentration profiles and the gradient energy coefficient in Cu-Pb

nanodroplets", *Phys. Rev. B* **76**, 094102 (2007).